Target Imaging and Backlighting Diagnosis

The case of an x-ray backlighting image of a CH-shell target imploded by the OMEGA Upgrade laser system has been calculated and analyzed. The goal is to obtain information on the conditions at peak compression, where the experimental constraints due to target self-emission and required spatial resolution are maximal. Particular attention is devoted to the problem of discriminating against the target self-emission. It is shown that this can be done by obtaining a monochromatic image at a single spectral line emitted by the backlighter. Additionally, the target self-emission image has useful signatures, which can be studied with or without a backlighter. Two experimental configurations for monochromatic imaging are discussed: (a) an x-ray microscope with a flat crystal monochromator, and (b) pinhole imaging in conjunction with a curved crystal monochromator. Useful images are obtained with simple (undoped) CH-shell targets and without the need for a short-pulse backlighter beam.

The method of x-ray backlighting offers some advantages over methods employing target emission for the study of compression and stability of laser-imploded targets. One advantage of backlighting over emission imaging is the potential to delineate the interface between the pusher and the fuel. This capability is more easily realized if the compressed fuel is relatively cold near the interface (i.e., a temperature gradient exists in the fuel). Such information can, in principle, provide a direct measure of compression and evidence of any shell distortion. Emission methods can only delineate the hot core, which may consist of the fuel as well as an indeterminate section of the pusher. An additional advantage is the ability to choose a short-enough backlighting wavelength (say, $\lambda < 3$ Å) to avoid too high an opacity; with emission, the interface region is often not hot enough to emit such short wavelengths.

An important ingredient in the backlighting schemes, as discussed below, is two-dimensional monochromatic imaging; this added feature can be likewise applied to, and enhance, methods based on target emission. Monochromatic imaging can be used to probe a particular layer in the target, which is doped with a suitable material. The imaging then involves a particular atomic transition of that material that gives rise to either monochromatic emission or absorption. However, in the case of backlighting, monochromatic imaging must be used even in the absence of a doped layer to overcome the background due to target emission.

When performing backlighting imaging, the self-emission of the imaged target is normally considered a hindrance and its suppression is considered desirable. In the test case studied here the backlighting and self-emission images happen to be of comparable intensity. This is an advantageous situation because the two image components provide complementary information on the compression and implosion uniformity.

Most backlighting experiments in the past were less challenging. Typically, they used softer backlighter radiation ($\lambda > 8$ Å) than we envisage using here. Softer radiation is heavily absorbed by the shell so it can only delineate the outer surface of the shell. This kind of measurement cannot yield reliable information on the compression or stability. Softer radiation is easier to produce in copious amounts, and the requirements on spatial resolution in imaging the outer surface of the shell are more moderate. Additionally, the problem of target self-emission in those earlier experiments was much less severe because the self-emission of a low-Z polymer target is mostly very weak, except for the emission from a highly compressed core, such as predicted for OMEGA Upgrade targets.

Case Study of Experimental Parameters

We discuss the feasibility of backlighting experiments, using the *LILAC* code for simulating a candidate OMEGA Upgrade target. The target is a polymer shell of 940-μm diam and 30-μm thickness, filled with 80 atm DT gas, and imploded by a trapezoidal pulse. The pulse rises linearly over a 0.1-ns period to 13.5 TW, then remains constant for 2.2 ns, before dropping linearly over a 0.1-ns period. *LILAC* results were used for simulating the expected backlight image for this test shot. Figure 58.1 shows the density and electron-temperature

profiles predicted for this target at peak compression. The shell material has been compressed to a mean radius of ~50 μm and thickness of ~30 μm, with a density in the range of ~10–50 g/cm³, corresponding to a $\rho\Delta r$ value of ~90 mg/cm². The electron temperature in the shell ranges from ~80 to ~1000 eV. Most of the backlight radiation absorption will occur within the colder, outer part of this compressed shell.
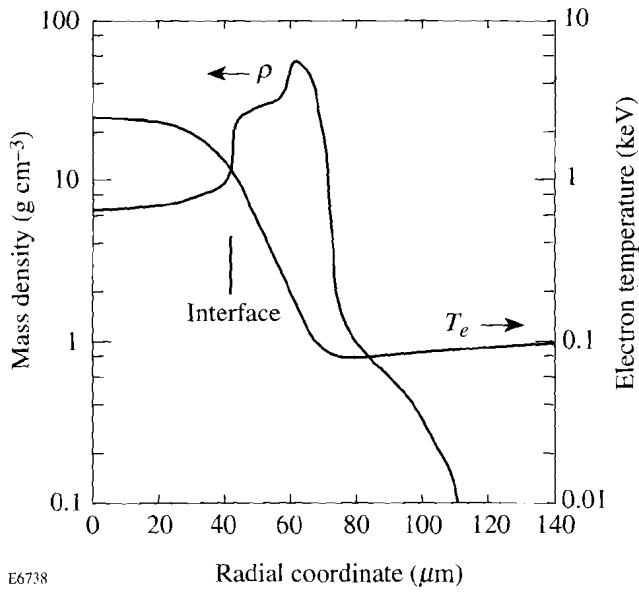
Figure 58.1

The density and electron-temperature profiles predicted by the *LILAC* code at peak compression for the case studied in this article.

Absorption Modeling

A simplified post-processor code was developed to calculate the transport of backlight radiation through the polymer target. The absorption at a wavelength λ in the CH material consists of two contributions: free-free (bremsstrahlung) and bound-free (photoionization); other absorption mechanisms (such as Compton scattering) are negligible for radiation of a few-keV photon energy. The free-free absorption coefficient at a frequency v (in cm^{-1}) is given by

$$k_{ff} = \left(4\pi z^2 e^6 g_{ff} \big/ 3^{3/2} hcm^2 v^3\right)\left(2m/\pi\kappa T\right)^{1/2} N_e N_i , \quad (1)$$

where g_{ff} is the free-free Gaunt factor (quantum correction). For a multispecies target, $z^2 N_e N_i$ is replaced by $N_e^2 \langle z^2 \rangle / \langle z \rangle$ in terms of species averages. The bound-free absorption coefficient for K-shell electrons (in cm^{-1}) in hydrogen-like ions is

given by

$$k_{bf} = \left(64\pi^4 z^4 me^{10} g_{bf} \big/ 3^{3/2} h^6 cn^5 v^3\right)\left(2m/\pi\kappa T\right)^{1/2} N_i , \quad (2)$$

where g_{bf} is the bound-free Gaunt factor, n is the principal quantum number of the absorbing level, and k_{bf} has to be calculated separately for each ionic species. For helium-like and higher ionic species, z^4 is replaced by $(z-\sigma)^4$, where σ is the Slater screening constant that equals[1] 0.3 for K-shell electrons. Neglecting the contribution to the opacity from L-shell and higher-shell electrons, the total opacity along various rays traversing the target can be now calculated, using the *LILAC*-predicted profiles of electron density and temperature through the target. To know the various N_i that go into the calculation of k_{bf} as well as into the z averages, we need first to calculate the distribution among the charge states (degrees of ionization). To calculate the charge-state distribution of carbon ions we make use of the LTE (local thermodynamic equilibrium) model. The LTE model becomes more valid as the plasma density increases and the temperature and the atomic charge Z decrease. These conditions indeed prevail within the cold, compressed part of the shell, made of low-Z polymer material. To verify the applicability of LTE we use the condition[2] given by Griem:

$$N_e > 7 \times 10^{18}\left(z^7/n^{17/2}\right)\left(\kappa T/z^2 E_H\right)^{1/2} \text{cm}^{-3}, \quad (3)$$

where E_H is the ionization energy of hydrogen (13.59 eV) and n is the lowest principal quantum number for which the level population is still in LTE with the continuum (i.e., whose population is related to that of free electrons by the Saha equation). For a typical temperature of 150 eV within the compressed shell, which is the principal absorber of backlighting radiation, and with $Z = 6$ and $n = 1$, Eq. (3) becomes $N_e > 3.2 \times 10^{24}$ cm^{-3}. This is well below the predicted values of $N_e \geq 1 \times 10^{25}$ cm^{-3}.

We use the Saha equation to calculate the distribution of carbon ions in the C^{+4}, C^{+5}, and C^{+6} charge states, while ignoring lower ionizations (which are negligible even at the lowest existing temperature, ~80 eV). The charge-state densities are then given by the set of equations:

$$\left(N_e N^{+6} / N^{+5}\right) = \left[2Z^{+6}(T)/Z^{+5}(T)\right]\left(2\pi m\kappa T/h^2\right)^{3/2}$$

$$\exp\left[-\left(E^{+5} - \Delta E^{+5}\right)/\kappa T\right], \quad (4)$$

$$\left(N_e N^{+5}/N^{+4}\right) = \left[2Z^{+5}(T)/Z^{+4}(T)\right]\left(2\pi m\kappa T/h^2\right)^{3/2}$$

$$\exp\left[-\left(E^{+4} - \Delta E^{+4}\right)/\kappa T\right],\qquad(5)$$

$$N^{+4} + N^{+5} + N^{+6} = N_C,\qquad(6)$$

where $Z(T)$ is the partition function, E^{+5} is the ionization energy of hydrogen-like carbon, E^{+4} that of helium-like carbon, and N_C is the total carbon ion density. The reduction in ionization energy ΔE is calculated by an approximation[3] to the theory of Stewart and Pyatt:[4]

$$\Delta E(eV) = 2.16 \times 10^{-7}\left(z/r_i\right)\left[\left(1 + x^3\right)^{2/3} - x^2\right],\qquad(7)$$

$x = r_D/r_i$, in terms of the Debye radius r_D and the interionic distance r_i:

$$r_D = \left[\kappa T/N_e\left(1 + \langle z \rangle\right)\right]^{1/2},\quad r_i = \left(3\langle z \rangle/4\pi N_e\right)^{1/3}.\qquad(8)$$

It should be noted that to calculate the charge distribution, we need to know $\langle z \rangle$ in Eq. (8), which calls for an iterative solution. To simplify the calculation we adopt the *LILAC* value of $\langle z \rangle$ for Eq. (8), since the reduction in ionization energy is needed only as a correction in the calculation of the charge distribution. Using the resulting densities, we can readily calculate the z averages, as well as the total bound-free opacity

$$k_{bf} = N^{+4}k_{bf,4} + N^{+5}k_{bf,5},\qquad(9)$$

where $k_{bf,4}$ is the bound-free opacity due to the helium-like carbon ion, and $k_{bf,5}$ due to the hydrogen-like carbon ion.

For the simulation we choose a backlight wavelength of 2.62 Å, corresponding to the $1s2p$–$1s^2$ line of Ti^{+20}. When irradiating a titanium backlighter target, this will be the strongest line, with a relatively low level of underlying continuum radiation.[5] We assume that the backlighter is irradiated by a single beam, identical to an OMEGA Upgrade beam with an energy of 500 J and the same pulse duration and shape as described above. We further assume a backlighter focal spot of 150-μm diam, giving rise to an irradiance of $\sim 1.4 \times 10^{15}$ W/cm^2. This diameter is sufficiently large for imaging the core at peak compression at which time the outer shell diameter is only ~ 120 μm. The optimal choice of wavelength for

a particular target implosion is one giving an opacity of ~ 1 in going through the target center at the desired time of probing. In this way the image will show the higher opacity going through the limb than through the center, thus delineating the outer as well as the inner surface of the cold pusher.

Monochromatic Absorption Images

In Fig. 58.2 we show examples of the predicted instantaneous backlighting images of the 2.62-Å line at various times during target compression. The abscissa is the lateral coordinate in the image plane, assuming unit magnification. The backlighting incident intensity is assumed to be unity. Target self-emission was not included in this calculation. The images assume that a monochromator was used for the detection; methods of monochromatization are described below. We see that titanium was a suitable choice for this target implosion; indeed, the opacity through the target center at peak compression [Fig. 58.2(e)] is ~ 0.9. As a result, the absorption through the target center is visibly lower than that through the limb. [The opacity through the limb in Fig. 58.2(e) is ~ 2.3.] The position of the minimum in the curve (maximum absorption) corresponds approximately to the fuel-shell interface; however, it is slightly larger than the interface radius. Thus, the minimum of the 2.87-ns frame [Fig. 58.2(e)] is at a radius of ~ 58 μm, while the interface (Fig. 58.1) is at a radius of ~ 45 μm. For homogeneous shells, the dip in the backlight image would correspond to a line of sight that is tangent to the fuel-shell interface; this direction corresponds to the longest chord through the target, therefore to the highest opacity. The main reason for this difference is the fact that the inner part of the shell is hot and has lower absorption (additionally, the density at this time peaks outside the interface radius). This difference yields an underestimate by a factor of ~ 2 in the derived compressed density. In cases where the electron-temperature profile is more centrally peaked, the absorption-profile minimum will yield a value closer to the correct density.

To minimize the smearing effect due to time integration, a framing camera can be employed behind the imaging device. In this case, only one frame can be easily accommodated because the various frames in a framing camera are recorded at various spatial directions, whereas here only one direction will yield the desired image: that given by the line connecting the main and backlighter targets. Figure 58.2 indicates that during a period of ~ 100 ps around peak compression (from ~ 2.8 to ~ 2.9 ns) the backlight image changes very little. Therefore, the method used to obtain time resolution need not achieve better than ~ 50-ps resolution (for probing peak compression).
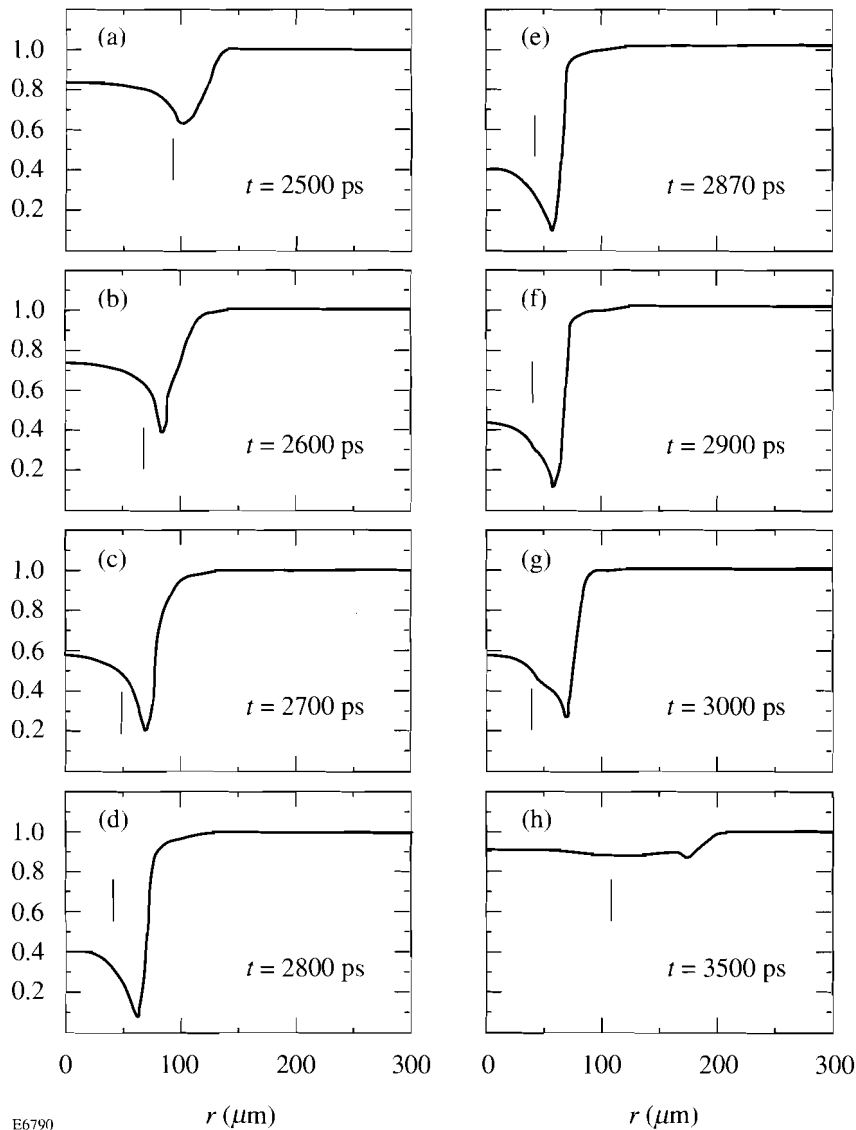
Figure 58.2

Examples of the predicted backlighting images at various times during the compression. The backlighting incident intensity was normalized to unity. Monochromatic backlighter was assumed at 2.62 Å (titanium). Target self-emission was not included. The vertical bars mark the fuel-shell interface.

Alternatively, the backlighter x-ray pulse can be shortened by using a polymer-coated Ti target, so that the Ti emission is delayed. To test this possibility we simulated the emission from a titanium target coated with varying thicknesses of polymer (CH) and irradiated with a single OMEGA Upgrade beam. The pulse shape was typical of those projected to be used in high-performance implosions: its total duration is 9 ns, it rises slowly first and then faster, until reaching a plateau of 0.3 TW from 8 to 9 ns, then dropping to zero. The total pulse energy is 0.5 kJ. This pulse shape is different than that described above, and used everywhere else in this work, and was chosen to verify x-ray pulse shortening even for this longer pulse. To

simulate a backlighter disk of 150-μm diameter, irradiated at 1.4×10^{15} W/cm^2, we assumed in the simulations a spherical target of 300-μm radius, irradiated at that irradiance. We summarize the results in Fig. 58.3, showing the x-ray emission from an uncoated titanium target, as well as from a titanium target coated with an 18-μm-thick CH layer. The x-ray emission is integrated over the 4.5- to 5-keV energy band, comprising mostly the Ti^{+20} resonance line at 4.73 keV. Even with no CH coating, the x-ray pulse is considerably shorter than the incident laser pulse because the early ("foot") part of the laser pulse is too weak to yield significant x-ray radiation within this energy band. A coating of 18 μm CH further

shortens the x-ray pulse to a width of ~160 ps, while reducing the x-ray power by only a factor of ~2. Thicker coatings cause precipitous reduction in x-ray power and are thus not useful.
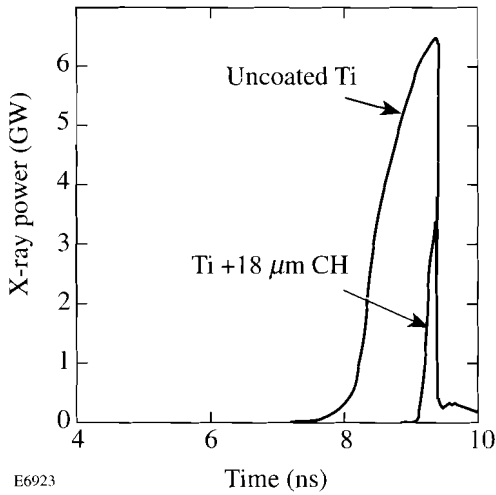

Figure 58.3
Simulated x-ray emission from an uncoated titanium target, as well as from a titanium target coated with an 18-μm-thick CH layer. The x-ray emission is integrated over the 4.5- to 5-keV energy band, comprising mostly the Ti^{+20} resonance line at 4.73 keV.

Emission Profiles

The backlighting images (such as in Fig. 58.2) should now be combined with the target self-emission profiles. We note that in LTE the local emission $\varepsilon(v)$ and the absorption coefficient $k(v)$ are related through Kirchhoff's law,[6] in terms of the blackbody function B_v:

$$\varepsilon(v) = k(v) B_v = \left(2hv^3/c^2\right)k(v)\Big/\left[\exp\left(hv/\kappa T\right)-1\right], \quad (10)$$

where κ is the Boltzmann's constant. Expressing Eq. (10) in explicit units,

$$\varepsilon\left(\frac{\text{keV}}{\text{keV ns cm}^3\,\Omega}\right)=3.13\times10^{22}\;\frac{k\left(\text{cm}^{-1}\right)\left[E(\text{keV})\right]^3}{\exp(E/T)-1}, \quad (11)$$

where Ω designates solid angle. The total spectral intensity emerging along a line of sight (in the x direction) at a distance y from the axial direction, due to both the backlighter as well as the target self-emission, is obtained by solving the radiation transport equation

$$I(v_0,y) = I_{BL}(v_0)\exp\left[-\int_{x_1}^{x_2}k(v_0,r)dx\right]$$

$$+ \int_{x_1}^{x_2}\varepsilon(v_0,r)\exp\left[-\int_{x}^{x_2}k(v_0,r')dx'\right]dx, \quad (12)$$

where $x_1 = -\left(R^2-y^2\right)^{1/2}$, $x_2 = -x_1$, $r = \left(x^2+y^2\right)^{1/2}$, $r' = \left(x'^2+y^2\right)^{1/2}$, R is the target radius, $I_{BL}(v_0)$ is the spectral intensity emitted by the backlighter at the line-center frequency v_0 (i.e., at 2.62 Å), and the local emission $\varepsilon(v)$ is given by Eq. (11). The resulting one-dimensional profile $I(v_0,y)$ is in reality, of course, circularly symmetric. Since we chose $I_{BL}(v_0)$ to correspond to the peak of the backlighting line, the profile calculated by Eq. (12) gives the highest possible contrast between the backlighting and the self-emission images. It will be realized only if the monochromator bandwidth is not larger than the spectral width of the backlighter line. For a wider bandwidth we sample a larger fraction of the continuous self-emission, but the intensity from the backlighter (assumed to be mostly in a single spectral line) will remain about the same, thus lowering the contrast.

We next estimate the backlighting irradiance $I_{BL}(v_0)$ at the 2.62-Å wavelength, the $1s2p$-$1s^2$ transition of Ti^{+20}. The assumed laser irradiance on the backlighter is 1.4×10^{15} W/cm^2, or 9.4×10^{21} keV/(ns cm^2). At this irradiance, the x-ray yield for producing the Ti^{+20} line at 2.62 Å can be conservatively taken[5] to be 0.03% into unit solid angle perpendicular to the target, giving an x-ray flux of 2.8×10^{18} keV/ (ns cm^2 Ω). To calculate the flux per unit photon energy, as explained above, this number has to be divided by the larger of the spectral line width and the instrumental width. The former is ~1.2 eV (see below), whereas a typical instrumental width would be ~4 eV. We finally obtain for the backlighting spectral flux at the frequency v_0 of line center

$$I_{BL}(v_0)=7.0\times 10^{20}\;\frac{\text{keV}}{\text{keV}/\left(\text{ns cm}^2\,\Omega\right)}. \quad (13)$$

Using this value and the plasma profiles calculated by the LILAC code (Fig. 58.1) we solve Eq. (12) numerically to obtain the combined image of backlighting and self-emission. The imaging device is assumed to have unit magnification and throughput.

We show in Fig. 58.4 the combined monochromatic image (at 2.62 Å) due to backlighting and self-emission at peak compression, intercepted by a monochromator crystal of 4-eV bandwidth. The curves are normalized to the spectral intensity of the backlighter, 7.0×10^{20} keV/(keV ns cm^2 Ω). We note that the two contributions (backlighting and self-emission) are of comparable intensity in this particular case. This indicates that without the use of a monochromator crystal the self-emission will dominate the image and render the method impractical. Thus, if instead of using a monochromator we were to use a filter, the intensity of the monochromatic back-lighting radiation (consisting of mostly a single spectral line) will remain about the same, but that of the continuous self-emission will greatly increase. For example, an appropriate filter for the 2.62-Å titanium line would be a 25-μm-thick titanium filter. Such a filter will produce a bandpass of an ~1-keV width (spanning the range ~4 to ~5 keV) as compared with the ~4-eV bandpass of the monochromator crystal.
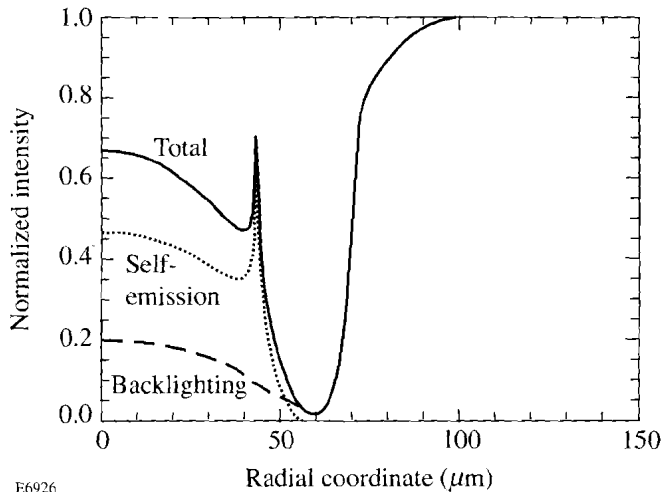

Figure 58.4

The combined image due to backlighting and self-emission at peak compression of an imploded CH shell. The image is calculated assuming a monochromatic detection at the $1s2p$–$1s^2$ line of a titanium backlighter ($\lambda = 2.62$ Å). The curves are normalized to a spectral intensity of 7.0×10^{20} keV/(keV ns cm^2 Ω).

The fact that both image components have comparable intensities makes the imaging method more powerful because information on both the cold shell as well as the interface can be simultaneously obtained. An underperforming target can be expected to show an absorption dip that is both shallower (because of a lower areal density $\rho\Delta r$ along the corresponding chord) as well as displaced to a larger radius (because of a lower compression). If the target performance greatly deviates from predictions (leading normally to a colder core), we may

have to employ softer radiation to see a comparable image. Also, the two-dimensional image can show long-wavelength perturbations of the spherical symmetry.

Of particular interest is the spike seen in the self-emission image at a radial distance of ~40 μm. This spike is emitted by the innermost surface of the CH shell and is due to the so-called "limb darkening," or the fact that the depth of a line-of-sight through the rim of a shell is longer than that through its center. In the complete two-dimensional image this spike will appear as a circular ring and will closely correspond to the fuel-shell interface. It provides therefore a direct measure of the achieved compression. Because of the potential usefulness of this spike we study its characteristics in some detail. The spike, if observable, can be used also in experiments with no backlighting. The image will not be then purely monochromatic, as in Fig. 58.4, but will instead be averaged over the transmitted spectrum of the filter. Our calculations also showed that averaging the image over the transmitted spectrum of a 25-μm-thick titanium filter hardly changed the self-emission image in Fig. 58.4.

The spike in Fig. 58.4 is spatially very narrow (~3 μm wide) because only the innermost surface of the CH shell is hot enough to emit the 4.73-keV radiation contributing to the image. As Fig. 58.1 shows, that temperature is in the range ~0.6–1.0 keV. If the core in an actual experiment is colder, the spike will be too weak to be seen, unless we choose softer radiation ($E < 4.7$ keV) for the imaging. Furthermore, an excellent spatial resolution is required. In Fig. 58.5 we show the result of a convolution of the emission image of Fig. 58.4 with an imaging device of 6-μm spatial resolution (and unit magnification). The spike is still seen, but poorer resolution renders it indistinct.

Figure 58.6 shows the self-emission of the test-case target at various photon energies. The motivation is to maximize the spike visibility; therefore, the backlighting part of the image was eliminated. The contrast of the spike with respect to the central peak maximizes in the 4- to 5-keV spectral range. To understand this we turn to Eqs. (11) and (12). The factor $k(E)$ E^3 appearing in Eq. (11) is essentially independent of E. By writing the derivative dE/dT from Eq. (11) we see that at higher photon energies the contrast between the spike and the central emission falls due to the $\exp(E/T)$ factor. This is because the central core is hotter than the shell interface region, and, when E/T is smaller, the exponential term increases more slowly with increasing E. At low photon energies, ab-
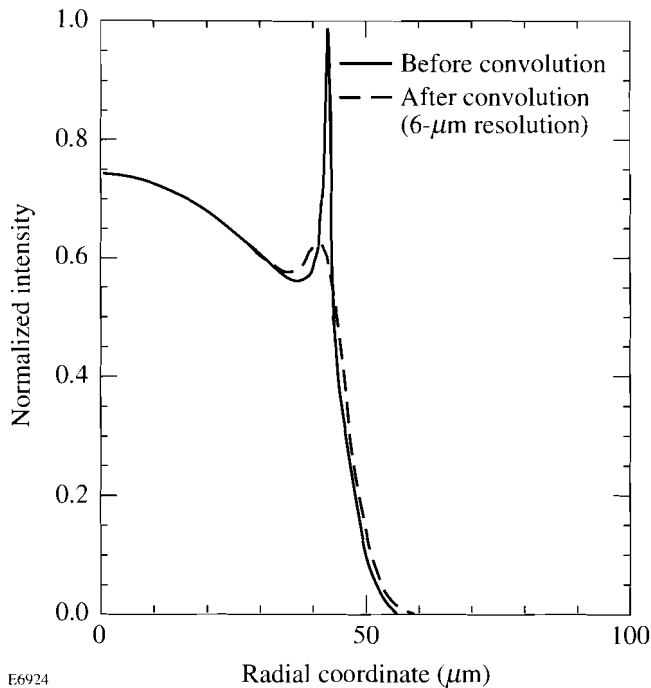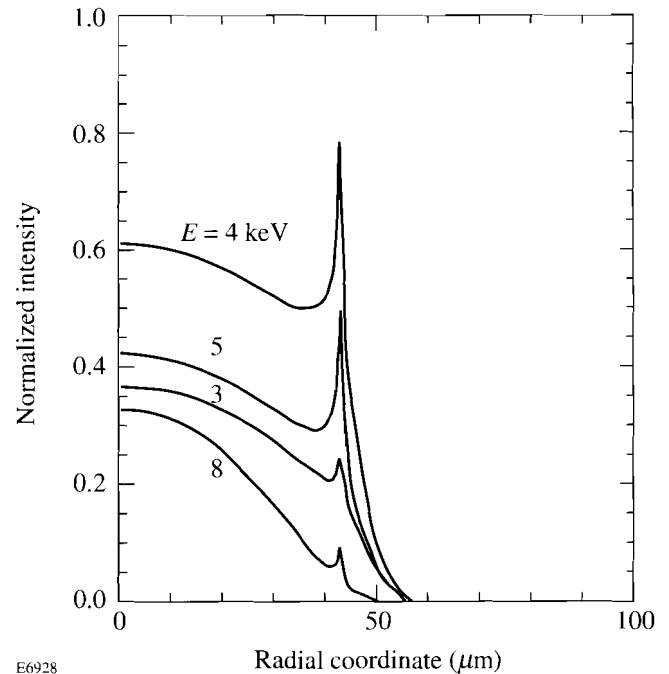
Figure 58.5
Convolution of the emission image of Fig. 58.4 with an imaging device of 6-μm spatial resolution (and unit magnification).

Figure 58.6
Self-emission profiles of the test-case target at various photon energies. The curves are normalized to a spectral intensity of 7.0×10^{20} keV/(keV ns cm^2 Ω).

sorption sets in and the limb-darkening effect disappears. The observed radiation from the hot part of the shell comes from the outer surface of that region and does not depend on its depth.

To maximize the spike emission it is instructive to know the relative contribution of the hydrogenic fuel and the CH shell to the emission profile. Figure 58.7 shows the emission profile of Fig. 58.4 with and without the hydrogenic fuel contribution. Even though the fuel has a lower nuclear charge than the carbon in the CH, a significant fraction of the central emission comes from the fuel because the fuel temperature is considerably higher than that in the shell. To increase the shell emission we may dope the CH shell with a higher-Z element. Irrespective of the detailed atomic physics of a high-Z dopant, its final effect is to increase the absorption coefficient and, through it, the local emission [see Eq. (11)]. To simulate doping we therefore multiply the absorption coefficient (and thereby also the emission coefficient) by a number m, which in Fig. 58.8 assumes the values 1, 2, 4, and 10. The only indeterminate information here is the quantity of a given type of dopant corresponding to each m. Figure 58.8 (calculated for a photon energy of 5 keV) shows that doping the shell cannot increase the contrast of spike to fuel emission because the

opacity through the region emitting the spike is not negligible (it is of order 1). For negligible opacities, the strong Z dependence of the absorption coefficient [Eqs. (1) and (2)] when substituted into Eq. (11) will result in much higher emission. However, when opacity is not negligible, the increase in the absorption coefficient, which also appears in the exponent of the attenuation [see Eq.(12)], will dominate and limit the spike intensity to that of a blackbody emitter. Additionally, the doped cold shell will further absorb the radiation emitted at the interface region. The length corresponding to this absorption is longer than through the center; this turns a flat-topped profile, characteristic of a high-opacity emitter, into the bell-shaped profiles for the high-m cases in Fig. 58.8.

Finally, we note that if the spike is still observed in the presence of mixing (which will be the case if the mixing is modest), it would permit an estimate of the degree of mixing. Mixing will raise the fuel emission (hence, the central peak in the image) relative to the spike emission. To simulate this effect, we show in Fig. 58.9 the emission profile when the fuel absorption coefficient is multiplied by $m = 1$, 2, and 4. Since the absorption coefficient of hydrogen is purely due to inverse bremsstrahlung, which depends on Z like Z^2 [see
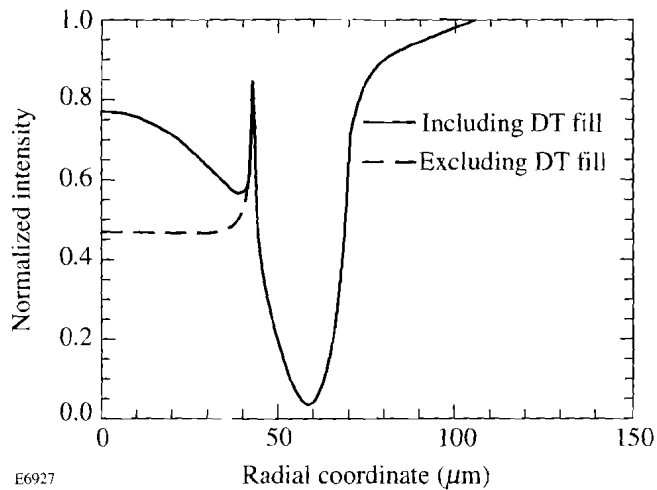
Figure 58.7
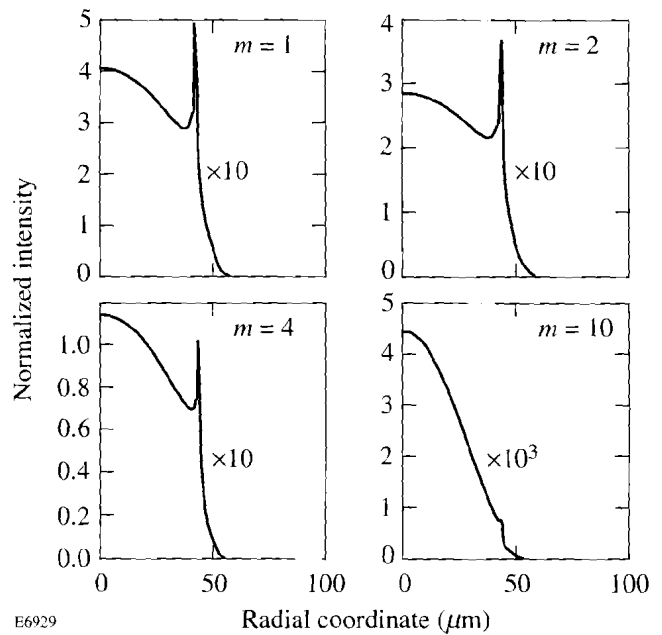Emission profile of Fig. 58.4 with and without the hydrogenic fuel contribution.

Figure 58.8
Simulation of shell doping with a high-Z additive. The absorption coefficient in the shell is multiplied by m. Detection is at 5-keV photon energy.

Eq. (1)], we can estimate the amount of CH mixed into the fuel for the $m = 4$ case as 8% by atom number. Much higher levels of mixing and shell distortion will make the spike disappear and render this method inapplicable.

Image Monochromatization

To improve the absorption-image visibility we assumed above that the backlighter emission is intercepted by a monochromator crystal that is angle adjusted for peak diffraction at 2.62 Å, the backlighting wavelength. The narrow reflection window of the crystal will greatly reduce the reflected broadband self-emission but will only slightly attenuate the single backlighting line. Roughly, the energy band diffracted by the crystal will be ~1 eV, as compared with a filter transmission window of ~1 keV. Thus, without a monochromator, the peak self-emission flux will be several orders of magnitude higher than the backlighter flux.

We now discuss in more detail the effect of introducing an x-ray reflecting crystal into the detection system. A problem we need to consider is the limitation on the field of view caused by the fact that the wavelength selection by a crystal is related to directional selection. In the dispersion direction, each wavelength can only be diffracted within a narrow angular diffraction range (of the order of ~10^{-4} rad) around the Bragg angle. However, the image generated by either a pinhole camera or a microscope can have a larger divergence than the acceptance angle of the crystal, in which case the monochromatic backlighter image may be clipped. For example, a 150-μm image size that is recorded by a pinhole at a distance
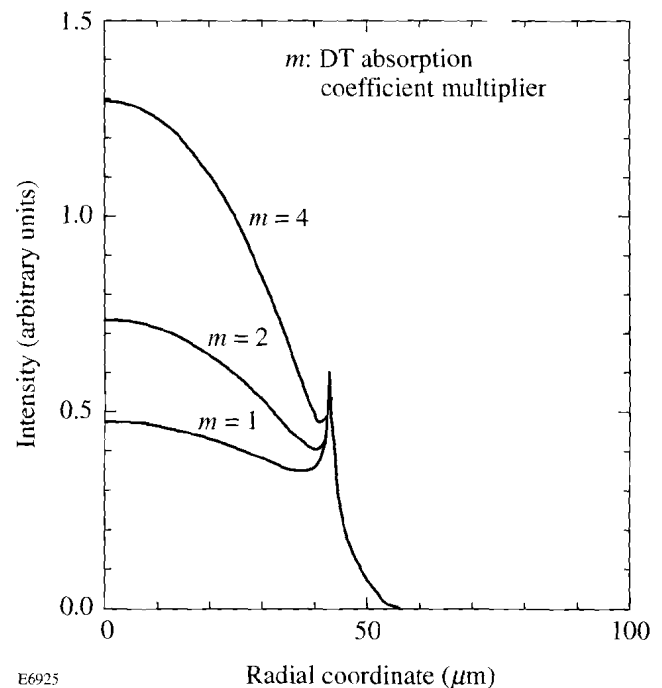

Figure 58.9
Emission profiles when the fuel absorption coefficient is multiplied by m, to simulate shell-fuel mixing. Detection is at 4.73-keV photon energy.

of 50 mm from the target corresponds to a divergence angle of 3×10^{-3} rad. Since an x-ray microscope is placed at longer distances (~200 mm), the divergence is smaller (~7×10^{-4} rad). To minimize the clipping problem we need to maximize the crystal acceptance angle $\Delta\theta_B$ for a given linewidth $\Delta\lambda$. To see the relationship between the two, we differentiate the Bragg condition $2d\sin\theta_B = \lambda$ and obtain

$$E/\Delta E = \lambda/\Delta\lambda = \tan\theta_B/\Delta\theta_B. \qquad (14)$$

The resolving power $\lambda/\Delta\lambda$ is a slowly varying function of the Bragg angle θ_B, so to maximize $\Delta\theta_B$ we should maximize θ_B. This requires selecting a crystal whose 2d spacing is only slightly larger than the relevant wavelength, so that the diffraction angle will be close to 90°. One appropriate choice for the 2.62-Å wavelength is topaz (303), of 2d spacing 2.712 Å, giving a Bragg angle of 74.5°. However, topaz has a high resolution (~6000), which makes $\Delta\theta_B$ narrow. If we choose Ge (111) of 2d = 6.545 Å and resolution ~3000, the Bragg angle for the 2.62-Å line will be only 23.5°. Using Eq. (10) we see that the gain of a factor of ~2 in $\Delta\theta_B$, with respect to topaz (because the resolution is lower), is outweighed by a decrease of a factor of 8 in $\tan\theta_B$.

The resolving power $\lambda/\Delta\lambda$ of topaz (303) was measured[7] to be ~10^4 in the range $\theta_B = 10°-40°$. Extrapolation to $\theta_B = 74°$ yields a resolving power of ~6×10^3, which from Eq. (14) corresponds to $\Delta\theta_B = 6 \times 10^{-4}$ rad. This divergence is smaller than that of the image of either the pinhole camera (4×10^{-3}) or the microscope (1×10^{-3}). However, the clipping problem is actually less severe due to the spectral linewidth $\Delta\lambda$. For example, the Doppler width of the 2.62-Å line in a titanium plasma of ion temperature $T_i = 500$ eV is $\Delta E_I = 1.2$ eV, which corresponds to $\Delta\theta_B = 9 \times 10^{-4}$ rad, about equal to the microscope image divergence. The finite spectral linewidth causes the crystal to reflect in each direction a slightly different wavelength within the linewidth. This eases the clipping problem but results in an intensity reduction of the order of 6/9 = 0.67. The field of view is still a problem for the pinhole-camera imaging, but not for microscope imaging.

The problem of limited field of view can be overcome by using a curved crystal (the Rowland circle geometry[8]), so that all rays forming the image have the same angle of incidence on the crystal. This is strictly true only for a Johansson-bent crystal. The resulting geometry is as follows: A pinhole is placed on the Rowland circle at a location corresponding to the backlighter wavelength (say, 2.62 Å). The target and the backlighter are placed outside the circle. Because of the limi-

tation on the solid angle occupied in the target vacuum tank, only small Bragg angles are feasible. The advantage of large Bragg angles described above disappears, but the focusing geometry compensates for this. A film is placed close to the crystal because farther from the crystal the focusing due to the curvature of the crystal eliminates the imaging. We have then two options for monochromatic imaging, both shown schematically in Fig. 58.10: (a) using an x-ray microscope with a flat crystal (topaz) interposed just in front of the recording medium, and (b) pinhole imaging coupled to a curved-crystal, Rowland-circle spectrometer. In (a) the Bragg angle is large (e.g., 74.5° for topaz), whereas in (b) the Bragg angle is small (12°-18° in our present design).
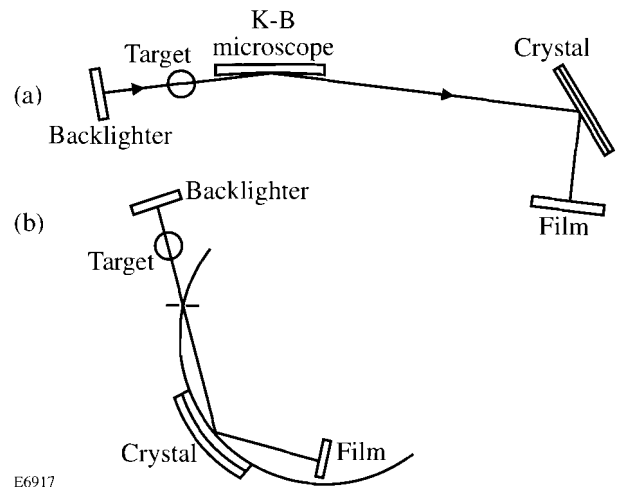

Figure 58.10
Schematic representation of two geometries for monochromatic backlighting: (a) Kirkpatrick-Baez x-ray microscope and a flat diffracting crystal; (b) pinhole imaging with a curved crystal on a Rowland circle.

The basis for imaging with a curved crystal, as stated above, is that all rays diverging from a single point on the Rowland circle and diffracted by a Johansson-type curved crystal fall on the crystal at the same Bragg angle. This assertion needs to be examined since the pinhole located on the Rowland circle [Fig. 58.10(b)] has a finite aperture. To find the divergence due to this finite size, we make use of the dispersion relation[8] of the Rowland spectrometer: $\Delta l = R \Delta\theta_B$, where R is the radius of curvature of the crystal (i.e., twice the radius of the Rowland circle) and $\Delta\theta_B$ is the change in the incidence angle on the crystal, corresponding to a travel Δl along the Rowland circle. A choice of $R = 60$ cm (corresponding to an actual spectrometer under construction at LLE) and $\Delta l = 10$ μm (corresponding to a pinhole of that diameter) yields $\Delta\theta_B = 1.67 \times 10^{-5}$ rad. This is smaller than the crystal accep-

tance angle $\Delta\theta_B = 3.5 \times 10^{-5}$ quoted above, meaning that a 10-μm-diam pinhole will not constitute the limiting factor in achieving monochromatic imaging. Instead, that limitation will be given by the imperfection of the crystal manufacturing and bending, as well as of the alignment.

We turn now to a comparison of sensitivity using both methods of imaging. A K-B microscope implemented at LLE[9] has a solid-angular aperture of 3×10^{-7}. For measuring the 4.73-keV titanium line, a gold coating is appropriate, having a reflection efficiency of ~0.3 over the range ~3.0–5.5 keV. The effective throughput (product of the angular aperture and the efficiency) is 9×10^{-8}. For the case of the pinhole-crystal method, a 10-μm-diam pinhole at 50 mm from the target, as assumed above, yields a solid-angular aperture of 4×10^{-8}, smaller than the aperture for the case of a K-B microscope. This is an additional advantage (in addition to the ease of aligning) in using a microscope-crystal combination, as opposed to using a pinhole with a curved crystal. It should be noted that there is no sensitivity gain due to the curvature of the crystal in the latter case because the film is placed very close to the crystal [Fig. 58.10(b)], before any significant focusing occurs. As explained above, such focusing would eliminate the imaging.

The effect of the monochromator bandwidth in reducing the continuum radiation participating in the image was already included (assuming a bandpass of 4 eV). We now calculate the crystal attenuation of the backlighting image for the experimental arrangement shown in Fig. 58.10(a). As it turns out, the results for the arrangement in Fig. 58.10(b) for a particular configuration are very similar.[10] The attenuation of the backlight image due to diffraction off a crystal monochromator is only by a factor of 2–5 because the beam forming the image is quasi-collimated when falling on the crystal.

We estimated above a resolving power of $\sim6 \times 10^3$ for the topaz crystal at 2.62 Å; this corresponds to an energy window of $\Delta E_c = 0.79$ eV. This happens to be smaller than the generic 4-eV bandwidth assumed in the calculations above. We first note that the divergence of the beam focused by the microscope and incident on the crystal is smaller than the angular reflection curve. If the crystal angle is properly tuned, all rays are approximately incident at the angle of the peak in the reflectivity curve. However, the actual reflectivity is not simply given by the peak reflectivity because of the finite spectral width of the 2.62-Å line. The reflection as a function of wavelength is simply related to the angular reflection curve

through the Bragg relation. This curve is approximately a Gaussian with peak reflectivity R_{max} and width ΔE_c. The spectral line shape can also be taken as a Gaussian of width ΔE_l. The effective crystal reflectivity will be lower than R_{max} because only rays of wavelength close to line center fulfill exactly the Bragg diffraction condition; the effective reflectivity is then given by the integral (assuming that the angle of incidence is the Bragg angle of peak reflectivity for the line-center wavelength):

$$R = \left(R_{max}/\Delta E_l \sqrt{\pi}\right) \int_{-\infty}^{\infty} \exp\left[-\left(\Delta E/\Delta E_l\right)^2\right]$$

$$\exp\left[-\left(\Delta E/\Delta E_c\right)^2\right] dE = R_{max}\Delta E_t/\Delta E_l, \quad (15)$$

where $\Delta E_t^{-2} = \Delta E_l^{-2} + \Delta E_c^{-2}$. For increasing ΔE, both the incident intensity (first Gaussian) is decreasing as well as the reflectivity (second Gaussian) because the detuning from line center is then larger. ΔE_t should not be construed as a total width; in fact ΔE_t is smaller than either ΔE_l or ΔE_c. As expected, when $\Delta E_l \ll \Delta E_c$, $R \approx R_{max}$. In the opposite case, when $\Delta E_l \gg \Delta E_c$, $R \approx R_{max} \Delta E_c/\Delta E_l$. In either case, the reflected intensity drops as we go to larger Bragg angles because (1) the peak reflectivity R_{max} drops for increasing θ_B and (2) ΔE_c also drops for increasing θ_B. Since the resolving power $E/\Delta E$ is usually almost constant as θ_B changes, it means that ΔE_c changes like $\sim 1/\sin\theta_B$. In the case of flat-crystal diffraction we are compelled to pay the price of reduced intensity to ensure a large enough field of view (by going to large Bragg angles, where $\Delta\theta_B$ is larger, even though ΔE_c is smaller). When using a curved crystal (Rowland spectrometer), the field-of-view problem is overcome because of the property of Rowland circle focusing, namely, that all rays diverging from a point on the circle fall on a Johansson-bent crystal at the same angle, enabling us to take advantage of the higher reflectivity at small Bragg angles. On the other hand, small Bragg angles are also mandated by the geometric constraints of the target vacuum chamber.

For the case of the topaz crystal, it was estimated earlier that $\Delta E_c = 0.79$ eV and $\Delta E_l = 1.2$ eV, yielding $R = (0.66/1.2)$ $R_{max} = 0.55\ R_{max}$. To estimate R_{max}, we extrapolate the data for the integrated reflectivity of topaz to 74° and find R_{int} $\sim 2 \times 10^{-4}$. Using the relationship $R_{int} \approx \Delta\theta_B \times R_{max}$ and the value of $\Delta\theta_B$ estimated above, we find $R_{max} = 0.33$ and,

finally, the effective reflectivity $R = 0.18$. This attenuation is the price we have to pay for using a monochromator crystal for reducing the contribution of target self-emission.

Conclusions

The expected backlighting and self-emission images of a particular CH target to be imploded on the OMEGA Upgrade are calculated for a variety of experimental parameters. The goal is to image the shell at peak compression with opacity of the order of 1. In this case, the image should delineate the inner surface of the imploded shell (or at least its colder portion), thus providing useful information on the compression and the symmetry. It is shown that to overcome the problem of target self-emission, the image has to be monochromatized with a diffracting crystal, and that the resulting attenuation of the backlighting image is not severe (by a factor of ~5). For the target studied, the two image components are then comparable in intensity, and both provide useful information on target behavior. Two experimental configurations for monochromatic imaging are described: (a) using a microscope and a flat crystal, and (b) using pinhole imaging and a curved crystal in the Rowland geometry. Useful images are obtained with simple (undoped) CH-shell targets and without the need for a short-pulse backlighter beam.

A particularly interesting feature is the appearance in the self-emission of a circular spike that closely delineates the fuel-shell interface but requires high spatial resolution to be observed. The optimization of its appearance is studied. Finally, it is shown that mixing of shell material into the fuel at up to ~10% by atom number might be diagnosable by the spike.

REFERENCES

1. H. A. Bethe and E. E. Salpeter, in *Quantum Mechanics of One- and Two-Electron Atoms* (Academic Press, New York, 1957), p. 295.

2. H. R. Griem, in *Plasma Spectroscopy* (McGraw-Hill, New York, 1964), p. 148, Eq. [6-55].

3. R. W. Lee, B. L. Whitten, and R. E. Stout II, J. Quant. Spectrosc. Radiat. Transfer **32**, 91 (1984).

4. J. C. Stewart and K. D. Pyatt, Jr., Astrophys. J. **144**, 1203 (1966).

5. B. Yaakobi, P. Bourke, Y. Conturie, J. Delettrez, J. M. Forsyth, R. D. Frankel, L. M. Goldman, R. L. McCrory, W. Seka, J. M. Soures, A. J. Burek, and R. E. Deslattes, Opt. Commun. **38**, 196 (1981); D. L. Matthews *et al.*, J. Appl. Phys. **54**, 4260 (1983).

6. H. R. Griem, *Plasma Spectroscopy* (McGraw Hill, New York, 1964), Eq. (7-6).

7. K. Gisselberg, Ark. Fys. **30**, 359 (1965).

8. B. Yaakobi, T. Boehly, and P. Audebert, Rev. Sci. Instrum. **61**, 1915 (1990).

9. Laboratory for Laser Energetics LLE Review **46**, NTIS document No. DOE/DP/40200-156, 1991 (unpublished), p. 91.

10. B. Yaakobi, F. J. Marshall, R. Epstein, and Q.Su, "Monochromatic Backlighting as a Laser-Fusion Diagnostic," to appear in the Journal of X-Ray Science and Technology.